# Exploration of the Lithium Storage Mechanism in Monoclinic Nb$_2$O$_5$ as a Function of the Degree of Lithiation

*Xilai Xue, Jakob Asenbauer, Tobias Eisenmann, Giovanni Orazio Lepore, Francesco d'Acapito, Silin Xing, Jens Tübke, Angelo Mullaliu, Yueliang Li, Dorin Geiger, Johannes Biskupek, Ute Kaiser, Dominik Steinle, Adele Birrozzi, and Dominic Bresser\**

Insertion-type Nb$_2$O$_5$ is a promising candidate for high-power lithium-ion anodes. Among the various polymorphs, monoclinic Nb$_2$O$_5$ (H-Nb$_2$O$_5$) is considered as one of the most promising materials. Herein, the impact of decreasing the lower cutoff potential, i.e., increasing the amount of lithium that is inserted into the crystal structure, from the commonly used 1.0 V versus Li$^+$/Li to 0.8 V and even 0.01 V is explored, yielding reversible specific capacities of 260, 280, and 400 mAh g$^{-1}$, respectively, at a specific current of 0.05 A g$^{-1}$. Remarkably, such increase in capacity does not come along with a deterioration of the cycling stability—at least initially. In fact, the comprehensive investigation of the reaction mechanism via *operando/ex situ* X-ray diffraction, *operando/ex situ* X-ray absorption spectroscopy, *ex situ* high-resolution transmission electron microscopy, and *operando* isothermal microcalorimetry reveals that the extension of the voltage range does not affect the crystal structure during the first couple of cycles, but there is a continuous evolution upon long-term cycling.

## 1. Introduction

With the envisioned goal of carbon neutrality, significant research efforts have been made to find suitable energy storage solutions for the transition to renewables only.[1–3] Owing to their high energy density, lithium-ion batteries (LIBs) are the technology of choice for portable electronic devices and (hybrid) electric vehicles.[4–6] At the negative electrode, the still mostly used active material is graphite, which has a high theoretical specific capacity of 372 mAh g$^{-1}$ and a very low de-/lithiation potential of about 0.1 V versus Li$^+$/Li, enabling high energy density at the full-cell level.[7] This low de-/lithiation potential, however, also favors lithium plating on the negative electrode, especially at high current densities and/or low temperatures.[7] As lithium plating results in unwanted side reactions with the electrolyte, thus triggering an accelerated ageing of the battery cell, and potentially bears the risk of short circuiting the cell when being plated as dendritic structures, fast charging remains a great challenge.[8,9] Alternatives such as Li$_4$Ti$_5$O$_{12}$ with a substantially higher de-/lithiation potential of about 1.6 V versus Li$^+$/Li provide potentially faster charging and very stable cycling performance,[10–12] but at the expense

X. Xue, J. Asenbauer, T. Eisenmann, S. Xing, J. Tübke, D. Steinle, A. Birrozzi, D. Bresser
Helmholtz Institute Ulm (HIU)
89081 Ulm, Germany
E-mail: dominic.bresser@kit.edu

X. Xue, J. Asenbauer, T. Eisenmann, S. Xing, J. Tübke, D. Steinle, A. Birrozzi, D. Bresser
Karlsruhe Institute of Technology (KIT)
76021 Karlsruhe, Germany

G. O. Lepore
Earth Science Department
University of Florence
50121 Florence, Italy

The ORCID identification number(s) for the author(s) of this article can be found under https://doi.org/10.1002/sstr.202300545.

F. d'Acapito
CNR-IOM-OGG c/o ESRF – The European Synchrotron
38043 Grenoble, France

S. Xing, J. Tübke
POLiS - Cluster of Excellence
Karlsruhe Institute of Technology (KIT)
89081 Ulm, Germany

A. Mullaliu
Department of Chemistry
KU Leuven
3001 Leuven, Belgium

Y. Li, D. Geiger, J. Biskupek, U. Kaiser
Central Facility for Electron Microscopy
Ulm University
89081 Ulm, Germany

of a relatively low energy density at the full-cell level owing to the lower theoretical specific capacity of 175 mAh g$^{-1}$ and the reduced cell voltage.[13]

Another potential insertion-type active material for the negative electrode is $Nb_2O_5$. $Nb_2O_5$ shows a rich structural chemistry and there are at least 12 polymorphs, which can be obtained by calcining the material at different temperatures.[14–17] These polymorphs include, among others, pseudohexagonal $Nb_2O_5$ (TT-$Nb_2O_5$), orthorhombic $Nb_2O_5$ (T-$Nb_2O_5$), tetragonal $Nb_2O_5$ (B-$Nb_2O_5$), monoclinic $Nb_2O_5$ (H-$Nb_2O_5$), and amorphous $Nb_2O_5$ (a-$Nb_2O_5$).[17–20] Among these polymorphs, H-$Nb_2O_5$ with the Wadsley–Roth shear structure was reported to deliver the highest initial capacity of around 250 mAh g$^{-1}$ in the voltage range from 1.0 to 3.0 V.[21] Nonetheless, it also showed an inferior rate capability and cycling stability compared to other polymorphs.[22] The de-/lithiation kinetics were improved, for instance, by applying a carbon coating on H-$Nb_2O_5$ nanoparticles, yielding a specific charge capacity of about 230 and 135 mAh g$^{-1}$ at a specific current of 0.1 and 6.0 A g$^{-1}$, respectively.[23] Similarly, nanocomposites of H-$Nb_2O_5$ and reduced graphene oxide provided reversible specific capacities of 190, 178, 166, and 150 mAh g$^{-1}$ at specific currents of 0.1, 0.25, 0.5, and 1.0 A g$^{-1}$, respectively.[24] Generally, it has been reported that the presence of planar defects favored higher capacities owing to a more open crystal structure, facilitating the insertion of lithium cations.[21,25] All these studies, though, focused on the relatively narrow voltage range from 1.0 to 3.0 V.

Herein, we explore the effect of lowering the lithiation cutoff potential to 0.8 and 0.01 V with a particular focus on the impact on the reaction mechanism. While the reversible capacity increases, it appears that the reaction mechanism remains the same. However, the comprehensive *ex situ* and *operando* characterization via X-ray diffraction (XRD), X-ray absorption spectroscopy (XAS), high-resolution transmission electron microscopy (HRTEM), and isothermal microcalorimetry (IMC) reveals that lowering the lithiation cutoff potential has an impact on the crystal structure in the long term.

## 2. Results and Discussion

The crystal structure of the as-synthesized H-$Nb_2O_5$ powder was verified by XRD, revealing a very good agreement with the JCPDS reference (card no. 37-1468) for the monoclinic structure, also referred to as Wadsley–Roth crystallographic shear structure (**Figure 1**a). The absence of additional reflections confirms that no other crystal structures are present. The subsequently recorded Raman spectrum (Figure 1b) is also well in line with the previous data reported for H-$Nb_2O_5$ and can be roughly divided into three regions[26–29]: The bands in the low wavenumber region from 100 to 150 cm$^{-1}$ are related to the Nb–Nb vibration modes, and the pronounced peaks at 123 and 135 cm$^{-1}$ are characteristic for a high degree of crystallinity. The bands in the medium wavenumber region from 150 to 350 cm$^{-1}$ have been
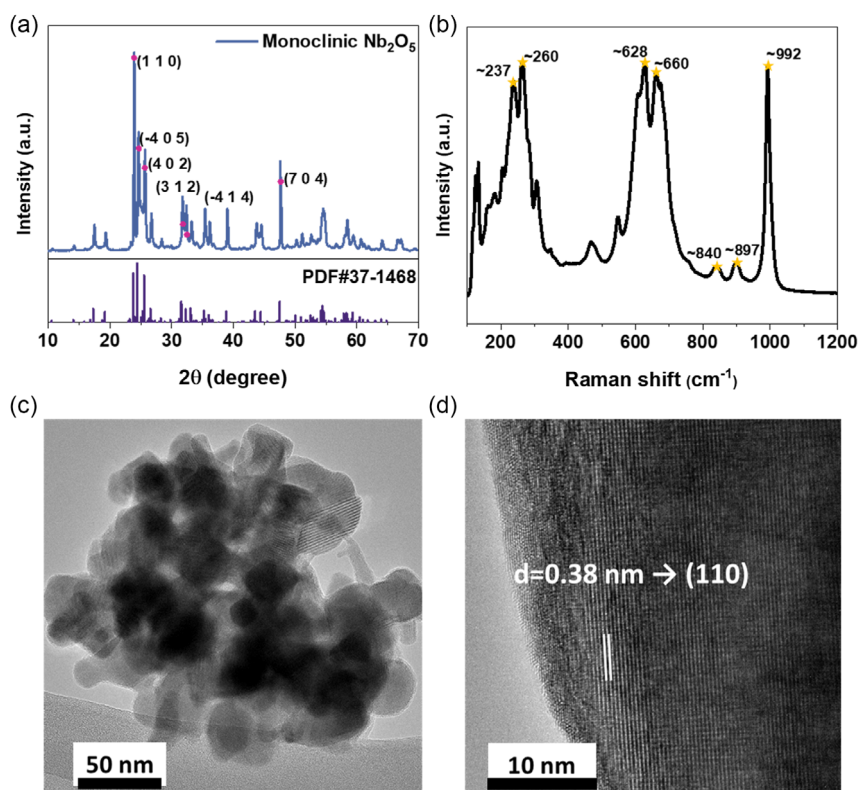


**Figure 1.** a) XRD pattern of H-$Nb_2O_5$ calcined at 1000 °C for 3 h under air. b) Raman spectrum of the pristine H-$Nb_2O_5$ powder. c) 300 kV TEM bright-field image overview image of H-$Nb_2O_5$ particles. d) 300 kV aberration corrected HRTEM lattice image of edge of a particle showing the (110) lattice spacing of H-$Nb_2O_5$ at 0.38 nm.

assigned to the Nb–O–Nb angle deformation, and the bands in the region from 400 to 800 cm$^{-1}$ are related to the Nb–O stretching vibration, including the two bands at 628 and 660 cm$^{-1}$, which are indicative of slightly distorted $NbO_6$ octahedra. The rather broad and less intense band at around 840 cm$^{-1}$ has been assigned to collinear Nb—O—Nb bonds formed by corner-shared octahedral $NbO_6$,[28] and the bands at 897 and 992 cm$^{-1}$ have been ascribed to the asymmetric and symmetric stretching modes of surface terminal Nb=O double bonds, respectively.[28,30] The particle size and crystallinity were further investigated by HRTEM, revealing a particle size of about 30–40 nm (Figure 1c) and a lattice spacing of 0.38 nm for the (110) lattice spacing (Figure 1d and S1, Supporting Information), thus corroborating the detection of the monoclinic structure by XRD.

Following this basic characterization, we prepared electrodes comprising the as-synthesized $H-Nb_2O_5$ as the active material. The Raman spectrum recorded for such electrodes (Figure S2, Supporting Information) is essentially the same as the one obtained for the pristine powder, confirming that the aqueous electrode processing did not have any impact on the crystal structure of the active material. For the electrochemical characterization, we first subjected these electrodes to galvanostatic cycling experiments in half-cells, i.e., with lithium-metal counter and reference electrodes, and varied the specific current from 0.05 to 20.0 A g$^{-1}$ as well as the lower cutoff potential from 1.0 to 0.8 V and 0.01 V while keeping the upper cutoff potential constant at 3.0 V. The results are shown in **Figure 2**a–c, and the corresponding dis-/charge profiles in Figure S3–S5, Supporting Information.

The comparison of the different cutoff potentials at varying specific currents revealed that the effect of lowering the upper cutoff potential to 0.8 V was rather small, becoming negligible at elevated currents up to about 0.5 A g$^{-1}$ (Figure 2a). When further lowering it to 0.01 V, however, the capacity was substantially higher. For instance, at a specific current of 0.1 A g$^{-1}$, when setting the lower cutoff potential to 0.01 V, it was about 370 compared to 250 mAh g$^{-1}$ with the lower cutoff potential set to 1.0 V. This trend persists also at elevated currents of, e.g., 5.0, 10.0, and 20.0 A g$^{-1}$, at which the reversible capacity was about 210, 180, and 140 mAh g$^{-1}$ for 0.01 V, while it was only about 125, 100, and 75 mAh g$^{-1}$ for 1.0 V, respectively. For all three cutoff potentials, though, the capacity at 0.2 A g$^{-1}$ after the C rate test was comparable to the capacity at 0.2 A g$^{-1}$ during the C rate test, indicating that the elevated C rates did not have a detrimental impact on the reversibility of the de-/lithiation. The comparison of the corresponding dis-/charge profiles (Figure S3, Supporting Information) revealed that the decrease in capacity at elevated currents largely resulted from the gradual shortening and eventual disappearance of the low-voltage dis-/charge plateau at about 1.1/1.2 V, while the plateau at about 1.6/1.7 V got shorter as well, but remained to some extent also at very high specific currents. Interestingly, the overall shape and the general trend were the same, independent from the lower cutoff potential.

When subjecting the electrodes to a constant specific current of 0.2 A g$^{-1}$ for 500 cycles, however, it became apparent that the cell with the highest cutoff potential of 1.0 V showed the most stable cycling at about 170 mAh g$^{-1}$, while the cell with the slightly lower cutoff potentially gradually faded, finally showing almost the same capacity after 500 cycles with about 180 mAh g$^{-1}$ as the one cycled with a higher cutoff of 1.0 V (Figure 2b). The cell with the lowest cutoff potential of 0.01 V
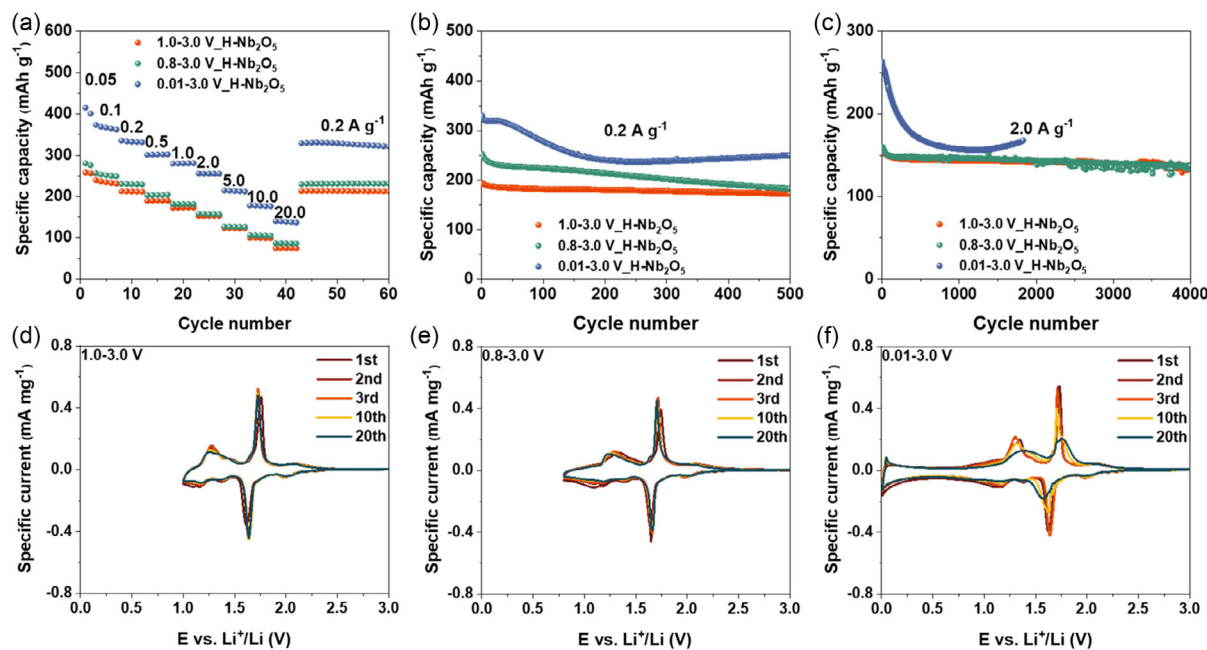


**Figure 2.** a–c) Galvanostatic cycling of the $H-Nb_2O_5$ electrodes in half-cell configuration with a lower cutoff potential of 1.0, 0.8, and 0.01 V: (a) at varying specific currents from 0.05 to 20.0 A g$^{-1}$, and subsequently at 0.2 A g$^{-1}$; (b) at a constant specific current of 0.2 A g$^{-1}$ after two formation cycles at 0.05 A g$^{-1}$; and (c) at a constant specific current of 2.0 A g$^{-1}$ after two formation cycles at 0.05 A g$^{-1}$. d–f) Cyclic voltammetry at a sweep rate of 0.1 mV s$^{-1}$ with an anodic reversing potential of 3.0 V and varying cathodic reversing potentials of (d) 1.0 V, (e) 0.8 V, and (f) 0.01 V. In all three cases, only the 1st, 2nd, 3rd, 10th, and 20th cycles are displayed for clarity reasons.

was initially providing a stable capacity for the first 30 cycles. Nonetheless, afterward the capacity decreased rather rapidly, before stabilizing at about 240 mAh g$^{-1}$ for the remaining cycles–even slightly increasing again to finally about 250 mAh g$^{-1}$ after 500 cycles. The inspection of selected dis-/charge profiles, presented in Figure S4, Supporting Information, shows that also in this case the capacity decrease is largely related to the vanishing low-voltage features in the range from 1.0 to 1.6 V, and the dis-/charge profiles of the cells with a cathodic cutoff potential of 1.0 and 0.8 V largely resemble each other. For the cell cycled with a cathodic cutoff potential of 0.01 V, though, the voltage plateau at about 1.6/1.7 V, ascribed to the phase transition from H-Nb$_2$O$_5$ to Li$_x$Nb$_2$O$_5$,[31] is getting increasingly sloped, indicating an increasing disorder of the crystal structure upon long-term cycling. When subjecting the cells to an elevated specific current of 2.0 A g$^{-1}$ for up to 4000 cycles (Figure 2c), only a very minor difference was found for the two cutoff potentials of 1.0 and 0.8 V. The specific capacity was about 142 mAh g$^{-1}$ (1.0 V) and around 146 mAh g$^{-1}$ (0.8 V) and the capacity retention was about 89% after 4000 cycles in both cases. Differently, in the case of the lowest cutoff potential, the capacity rapidly decreased, before stabilizing after about 1000 cycles. The comparison of the corresponding dis-/charge profiles in Figure S5, Supporting Information, showed that the shape of the dis-/charge profiles was essentially the same for 1.0 and 0.8 V, but in the latter case, an increasing polarization was observed. In the case of 0.01 V, in fact, the dis-/charge profiles were substantially changing upon cycling, with a shortening voltage plateau and greatly increasing polarization, thus further indicating a deterioration of the crystal structure upon long-term cycling.

These substantially more pronounced changes became also apparent from the comparison of the cyclic voltammetry data, as presented in Figure 2d–f. While the major features are initially the same for all cathodic reversing potentials, remaining basically the same for 1.0 V (Figure 2d) and 0.8 V (Figure 2e), there was a substantial evolution observed in the case of 0.01 V (Figure 2f). The peaks of the major redox couple at about 1.6 and 1.7 V, for instance, largely decreased in intensity, got broader, and the peak separation increased, further corroborating substantial structural changes in the active material.

To investigate the de-/lithiation mechanism as a function of the lower cutoff potential in more detail, we carried out a set of complementary *operando* and *ex situ* characterization techniques. In a first step, we conducted *operando* XRD for the three different lower cutoff potentials. The results for 0.01 V are depicted in **Figure 3**a, and the results for 1.0 and 0.8 V are presented in Figure S6a,b, Supporting Information, respectively.

The initial diffractogram prior to any cycling was in line with the diffractogram of the pristine powder, and the corresponding lattice planes are indicated on the top of the characteristic reflections. When starting the discharge process, the cell voltage rapidly dropped to the voltage plateau at about 1.6 V. The presence of a voltage plateau indicates a two-phase equilibrium, corresponding to the phase transition from monoclinic Nb$_2$O$_5$ (JCPDS card no. 37-1468) to monoclinic Li$_{1.9}$Nb$_2$O$_5$ (JCPDS card no. 37-0976). Subsequently, the reflections shifted to lower $2\theta$ angles, indicating a solid-solution-type lithiation along with an expansion of the lattice. Upon further lithiation, starting from about 1.0 V, a

second phase transition was observed—in good agreement with the second (sloped) voltage plateau at about 1.1 V observed in Figure S3, Supporting Information, for instance. The slightly lower voltage and less pronounced (sloped) plateau presumably originates from the different cell setup. This (sloped) voltage plateau is attributed to the transition from Li$_{1.9}$Nb$_2$O$_5$ to Li$_y$Nb$_2$O$_5$ ($y > 2$). We could not yet identify the crystal structure of this new phase, but it appears noteworthy that the reflections shifted only slightly to lower $2\theta$ angles throughout the further lithiation, suggesting that this new crystal structure provides sufficient space to accommodate significantly more lithium cations and/or that the further lithiation is (in part) pseudocapacitive in nature. Considering the overall lithiation capacity in this and the previous experiments, we may assume that the final phase has a composition of about Li$_4$Nb$_2$O$_5$.

The structural changes and reaction mechanisms appeared very reversible upon delithiation, with a much more pronounced voltage plateau at about 1.2 V for the transition back to the monoclinic Li$_{1.9}$Nb$_2$O$_5$ phase. This phase transition was followed by a solid-solution regime, and eventually at around 1.7 V the second voltage plateau, which is related to the phase transition from monoclinic Li$_{1.9}$Nb$_2$O$_5$ to H-Nb$_2$O$_5$. In fact, the diffractogram at 3.0 V very well resembled the diffractogram of the electrode prior to any cycling, indicating a high reversibility of the lithiation reaction and the structural changes involved. In Figure S7, Supporting Information, selected diffractograms are depicted, which were obtained upon discharge at about 1.0 and 0.01 V, as well as upon charge at around 1.0 and 3.0 V, along with the relevant JCPDS reference data and an indication of the new reflections appearing for the highly lithiated Li$_y$Nb$_2$O$_5$ ($y > 2$) phase.

The *operando* XRD data recorded for the two higher cutoff voltages of 1.0 V (Figure S6a, Supporting Information) and 0.8 V (Figure S6b, Supporting Information) showed essentially the same features, indicating that the reaction mechanism is independent from the lower cutoff voltage. It may be noted, though, that the newly formed Li$_y$Nb$_2$O$_5$ ($y > 2$) phase became apparent only for the lower cutoff voltage of 0.8 V, revealing that the second-phase transition did not occur for the higher cutoff voltage of 1.0 V—at least not to an extent that would allow its detection in the *operando* XRD results.

To obtain further insights into the structural changes occurring upon deep lithiation to 0.01 V, we conducted *operando* and *ex situ* XAS on the H-Nb$_2$O$_5$ electrodes. The *operando* XAS data for the Nb K-edge are presented in Figure 3b, revealing a continuous shift of the pre-edge and edge position toward lower energies upon lithiation, and eventually a disappearance of the pre-edge feature. Such shift is well in line with the reduction of the niobium oxidation state as a result of the Li$^+$ cation insertion. Upon delithiation, this shift was fully reversible, being in very good agreement with the *operando* XRD results. For a closer inspection of the changes, we coupled the *operando* experiment with *ex situ* measurements at selected states of discharge and charge, as depicted in Figure S8, Supporting Information. The results are shown in Figure 3c. Generally, the trend was the same as observed for the *operando* experiment, i.e., the edge position shifted to lower energies and the pre-edge peak gradually shifted and eventually disappeared, indicating the reduction of the niobium oxidation state. This reduction presumably comes along
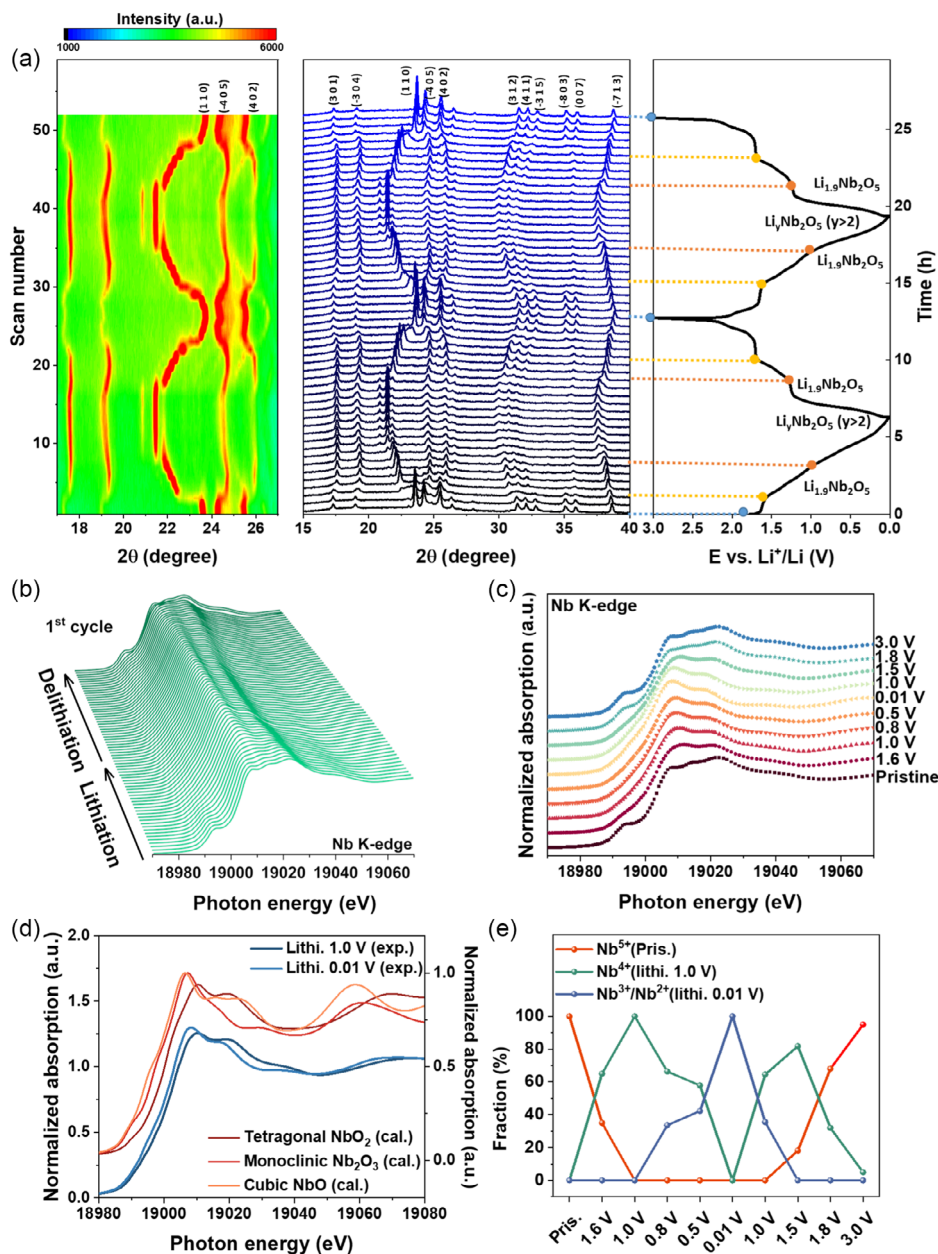
**Figure 3.** a) *Operando* XRD data for a lower cutoff potential of 0.01 V, including the contour plot (left), the corresponding diffractograms (middle), and the dis-/charge profiles for the first two cycles (right). The specific current was 0.08 A g$^{-1}$. b) *Operando* XANES spectra at the Nb K-edge for the first cycle. c) *Ex situ* XANES spectra at the Nb K-edge at various states of discharge and charge. d) Comparison of the experimental and *ab initio* simulated XANES spectra at the Nb K-edge. e) Outcome of the LCF fitting of the *ex situ* XAS data recorded at different states of discharge and charge, yielding a rough quantification of the presence of the different niobium oxidation states.

with a modification of the local geometry and crystal structure around the niobium cations, as indicated by the evolution of the overall shape of the spectra. The comparison of the X-ray absorption near edge structure (XANES) part of the spectra with *ab initio* calculated spectra for tetragonal $NbO_2$, monoclinic $Nb_2O_3$, and cubic NbO indicated that the oxidation state of niobium in the fully lithiated state at 0.01 V was between +2 and +4 (Figure 3d). Interestingly, the *ex situ* spectrum recorded for the sample stopped at 1.0 V resembled more the shape of the

calculated XANES spectrum for tetragonal $NbO_2$, while the *ex situ* spectrum recorded for the sample stopped at 0.01 V showed rather some similarities with a combination of the calculated XANES spectra for monoclinic $Nb_2O_3$ and cubic NbO, suggesting a further reduction of the niobium oxidation state and structural changes, as also observed by *operando* XRD. To provide an estimation of a more quantitative analysis, we performed linear combination fitting (LCF) of the experimental data (Figure 3e). As reference for the different oxidation states, we used the

**ADVANCED
SCIENCE NEWS**

www.advancedsciencenews.com

**small
structures**

www.small-structures.com

spectra recorded for the pristine electrode ($Nb^{5+}$), an electrode that was lithiated to 1.0 V ($Nb^{4+}$), and an electrode that was lithiated to 0.01 V (mixed $Nb^{2+}/Nb^{3+}$). The fractional sum of these components was constrained to unity and the R factor was below 0.004, indicating a good fit of the data. Based on this fit, at 1.6 V, for instance, upon lithiation, the fraction of $Nb^{5+}$ was still about 35%, while at 0.8 V around 65% of the niobium was present as $Nb^{4+}$ and 35% as $Nb^{2+}/Nb^{3+}$. These results showed that lowering the cathodic cutoff potential from 1.0 to 0.8 V results in a significant fraction of $Nb^{2+}/Nb^{3+}$, along with the structural changes found earlier, which provides an explanation for the less stable long-term cycling at moderate specific currents (Figure 2b).

Given that this effect got increasingly pronounced upon continuous de-/lithiation, we conducted in a next step an *ex situ* XRD analysis of electrodes subjected to 50, 200, and 500 cycles using the three different lower cutoff potentials. The *ex situ* XRD data are presented in **Figure 4** and the corresponding dis-/charge profiles are shown in Figure S9, Supporting Information. After 50 cycles, the crystal structure remained essentially the same as for the pristine electrodes. For a lower cutoff potential of 1.0 V, this was also true after 200 and 500 cycles (cf., Figure 4a–c). For the slightly lower cutoff potential of 0.8 V, a minor decrease in intensity was observed (cf., Figure 4d–f), indicating a slight decrease

in crystallinity. For 0.01 V, however, a rather substantial decrease in intensity was found (cf., Figure 4g–I; note also the different scale in Figure 4i), revealing that the continuous and much more extensive de-/lithiation led to a greatly increasing disorder of the initial crystal structure.

These findings were corroborated by *operando* and *ex situ* XAS during/after the 200th cycle (Figure S10, Supporting Information). In fact, the *operando* experiment during the 200th cycle (Figure S10a, Supporting Information) reveals essentially the same trend as during the first cycle (Figure 3b), but the direct comparison of the spectra recorded in the fully delithiated state with the one obtained after the first cycle (Figure S10b, Supporting Information) revealed some differences. The intensity of the pre-edge feature (A), which is correlated with the degree of distortion of Nb coordination,[32–35] was markedly reduced. This is compatible with a more centrosymmetric coordination of Nb, suggesting that Nb is hosted in more regular octahedra compared to the highly distorted sites of the starting material. Furthermore, features on the main edge crest (B and C) appear rather blunted compared to the spectrum after the first cycle. According to references[32–35], features B and C are related to single- and multiscattering paths of the photoelectron around Nb involving first (C) and second (B) nearest neighbors,
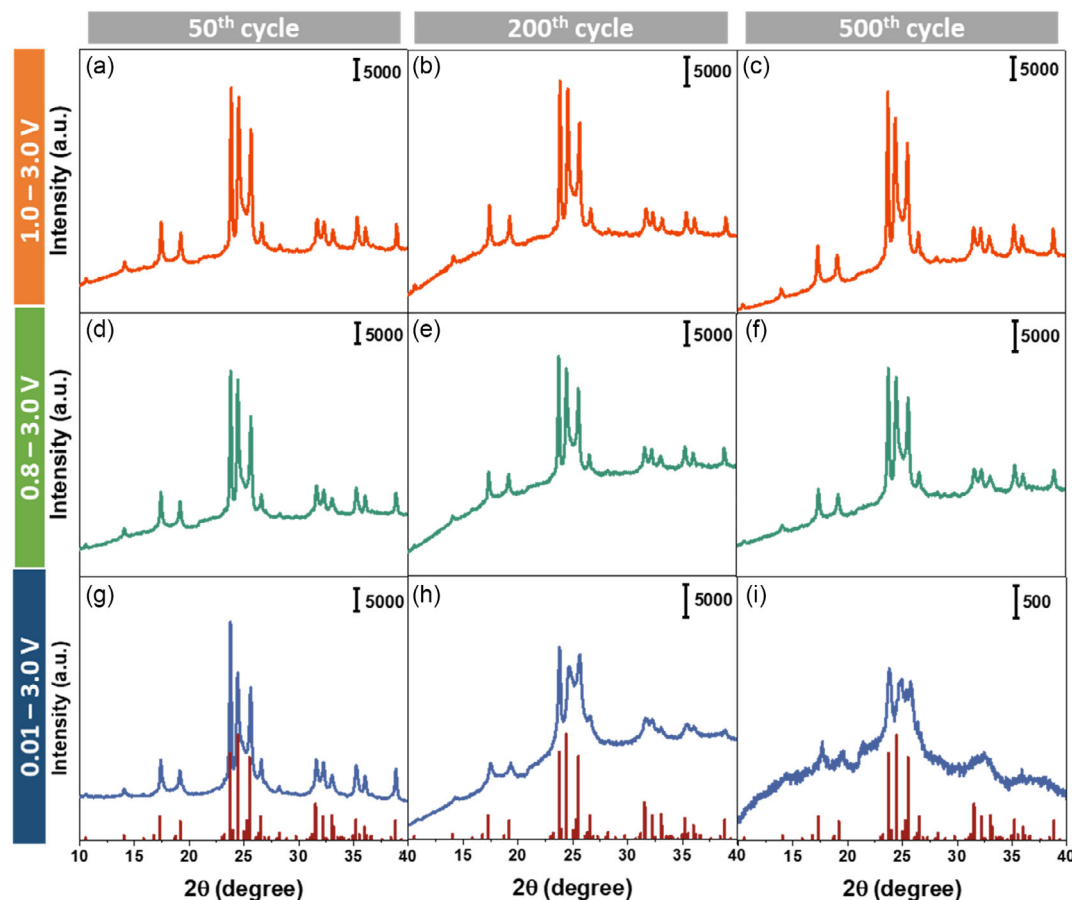


**Figure 4.** *Ex situ* XRD patterns recorded for H-Nb$_2$O$_5$ electrodes cycled with a lower cutoff potential of a–c) 1.0 V, d–f) 0.8 V, and g–i) 0.01 V and subjected to 50, 200, and 500 cycles (from left to right). The specific current was 0.05 A g$^{-1}$ in the first two cycles and 0.2 A g$^{-1}$ for the subsequent cycles. The electrodes were recovered in the fully delithiated state at 3.0 V.

**ADVANCED
SCIENCE NEWS**
www.advancedsciencenews.com

**small
structures**
www.small-structures.com

respectively, and tend to disappear in the case of a distorted local structure, which is well in line with the *ex situ* XRD results.

To further confirm these findings, we carried out an *ex situ* HRTEM investigation of electrodes subjected to 500 cycles with the different cathodic cutoff potentials (**Figure 5**). All three samples showed an amorphous layer at the particle surface, which might be related to the formation of the solid electrolyte interphase (SEI). Moreover, we observed the characteristic lattice spacing of, for instance, 0.36 nm ($-4\ 0\ 5$) and 0.51 nm ($3\ 0\ 1$) for the samples cycled with a cathodic cutoff of 1.0 (Figure 5a) and 0.8 V (Figure 5b), respectively. These findings corroborated the well-maintained crystallinity. Also, for the sample subjected to 500 cycles with the lowest cutoff of 0.01 V (Figure 5c), we still

detected the lattice spacing of 0.28 nm ($-4\ 1\ 4$), but the overall appearance was more amorphous compared to the other two samples, being well in line with the *ex situ* XRD results.

Finally, we explored also the impact of the variation of the lower cutoff potential with regard to the potential application of $H-Nb_2O_5$ in lithium-ion cells. For this purpose, we combined the experimentally obtained dis-/charge profiles and specific capacities with a theoretical $LiNi_{0.5}Mn_{1.5}O_4$ cathode, assuming a constant de-/lithiation potential of 4.7 V versus $Li^+/Li$ and a specific capacity of 140 mAh g$^{-1}$.[11,36,37] The combination of these two electrodes for the different lower cutoff potentials is displayed in **Figure 6**a–c. The calculation of the semitheoretical specific energy, taking into account only the mass of the two
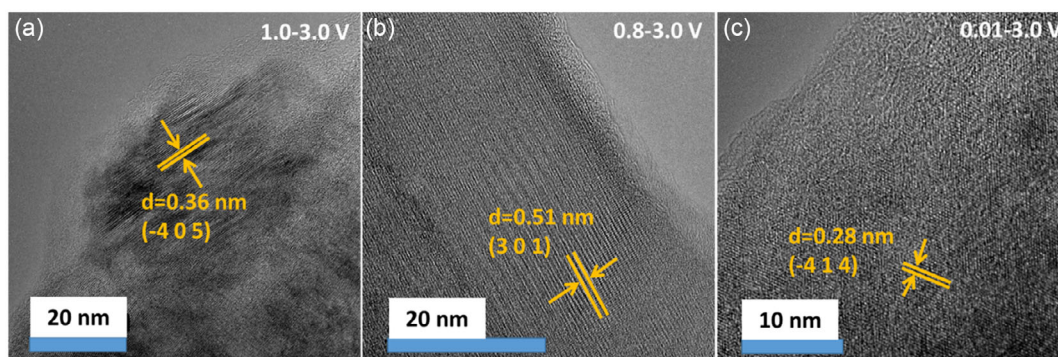


**Figure 5.** *Ex situ* 300 kV aberration-corrected HRTEM images of $H-Nb_2O_5$ electrodes subjected to 500 cycles with a lower cutoff potential of a) 1.0 V, b) 0.8 V, and c) 0.01 V.
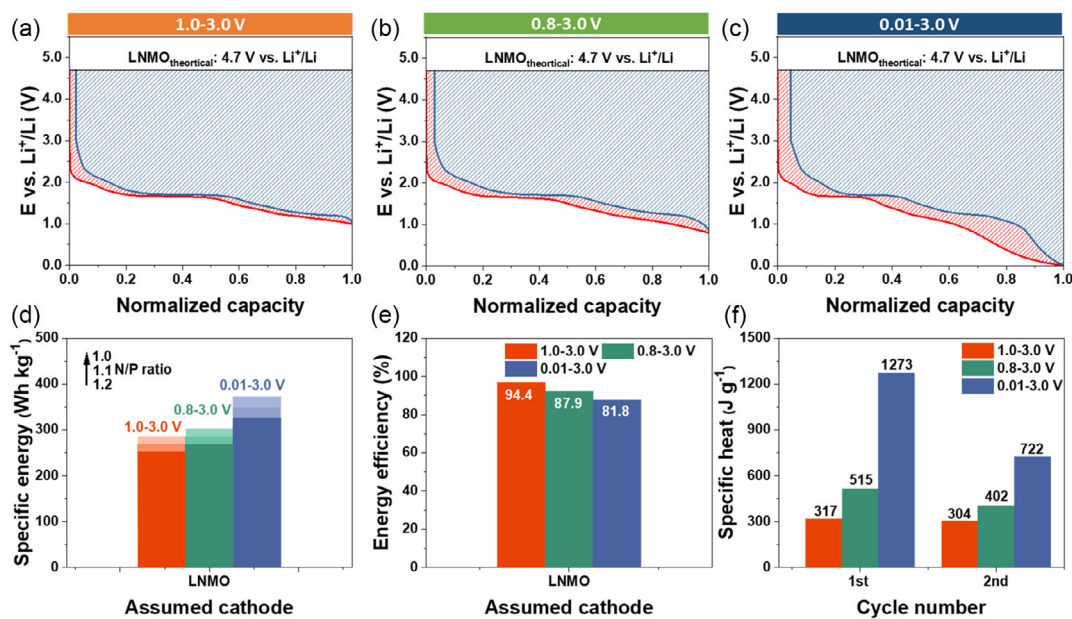


**Figure 6.** Evaluation of "semitheoretical" lithium-ion full cells based on the experimental data of $H-Nb_2O_5$ anodes and theoretical $LiNi_{0.5}Mn_{1.5}O_4$ cathodes with a de-/lithiation potential of 4.7 V versus $Li^+/Li$ as a function of the lower cutoff potential: a–c) Plot of the corresponding dis-/charge profiles with an indication of the calculation of the specific energy and EE for a lower cutoff potential of (a) 1.0 V, (b) 0.8 V, and (c) 0.01 V. d) Comparison of the calculated semitheoretical specific energy for the three different cutoff potentials and varying N:P ratios. e) Comparison of the EE for the semitheoretical full cells. f) Comparison of the total specific heat as determined by *operando* isothermal calorimetry for the $H-Nb_2O_5$ electrodes cycled with lithium-metal counter electrodes and the three different cathodic cutoff voltages ($T = 25\ °C$).

**ADVANCED
SCIENCE NEWS**

www.advancedsciencenews.com

**small
structures**

www.small-structures.com

active materials and assuming varying N:P ratios of 1.0, 1.1, and 1.2, yielded values well above 300 Wh kg$^{-1}$ for the lowest cutoff potential of 0.01 V, values of around 300 Wh kg$^{-1}$ for 0.8 V, and values (well) below 300 Wh kg$^{-1}$ for 1.0 V (Figure 6d).

These results highlight that a lower cutoff potential might be detrimental for the cycling stability, but potentially beneficial for the specific energy. In fact, the maximum value for 0.01 V and an N:P ratio of 1.0 reached 374 Wh kg$^{-1}$ (and slightly lower values when increasing the N:P ratio to 1.1 or 1.2, as indicated by the arrow in Figure 6d). Given that the cathode active material mass loading might be sufficiently high in the lithium-ion cell, this would render the use of lower cutoff potentials for, e.g., pulsed discharge steps potentially advantageous. The plot of the semi-theoretical full cells in Figure 6a–c, however, also showed that the overall energy efficiency (EE), i.e., the product of the voltage efficiency and the Coulombic efficiency, decreased when lowering the cathodic cutoff, owing to a greater voltage hysteresis between the lithiation and delithiation process. The calculation of the EE yielded values of 94.4%, 87.9%, and 81.8% for 1.0, 0.8, and 0.01 V, respectively (Figure 6e), revealing a clear benefit of the elevated cutoff potential, in addition to the greater cycling stability.

As the EE is closely related to the heat evolution of the cell, we eventually conducted *operando* IMC on H-Nb$_2$O$_5$ electrodes coupled with lithium-metal counter electrodes in coin cells, setting the lower cutoff voltage to 1.0, 0.8, and 0.01 V. The comparison of the total specific heat evolving during the first and second cycle is depicted in Figure 6f. As expected from the comparison of the EE, the heat evolution was the greatest for a lower cutoff voltage of 0.01 V and substantially lower for the two other cutoff voltages—and the lowest for the highest cutoff of 1.0 V. A detailed plot of the heat evolution along with the corresponding dis-/charge profiles during the first cycle is presented in **Figure 7**. The heat evolution features observed for the cutoff voltage of 1.0 V (Figure 7a,b) and 0.8 V (Figure 7c,d) were generally very similar, reflecting the earlier discussed charge storage mechanism. We divided the lithiation process in two regions (A) and (B), i.e., up to the end of the voltage plateau at about 1.7 V (A) and after the voltage plateau (B). In region (A), two minor exothermic peaks were observed that are associated with the initial sloped decrease in voltage and the onset of the voltage plateau, reflecting the initial solid-solution regime and the onset of the phase transition from H-Nb$_2$O$_5$ to Li$_{1.9}$Nb$_2$O$_5$ along the
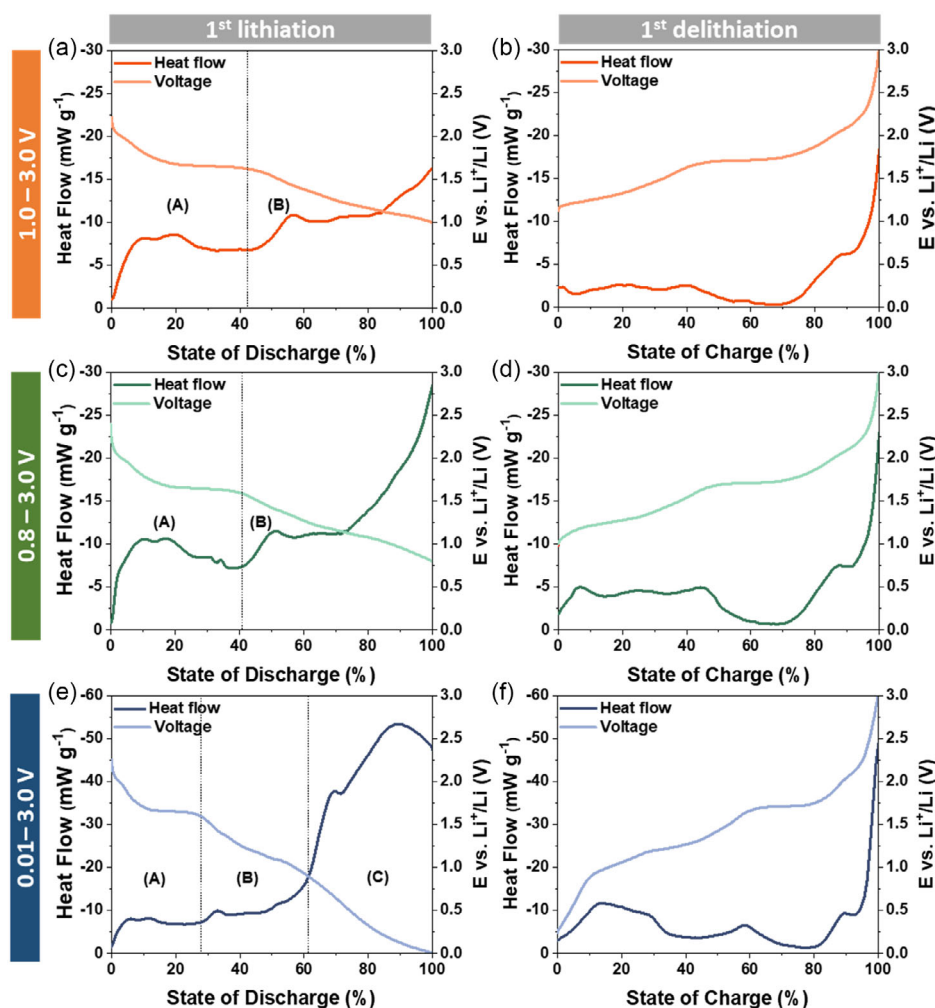


**Figure 7.** *Operando* IMC: Plots of the total heat flow and lithiation (left) and delithiation (right) profiles of the first cycle for H-Nb$_2$O$_5$ electrodes cycled versus lithium-metal counter electrodes with a lower cutoff voltage of a,b) 1.0 V, c,d) 0.8 V, and e,f) 0.01 V. The specific current was 50 mA g$^{-1}$ ($T = 25$ °C).

voltage plateau, respectively. Subsequently, in region (B), shortly after the voltage plateau another exothermic peak was observed that has been assigned to the onset of the second-phase transition from $Li_{1.9}Nb_2O_5$ and $Li_yNb_2O_5$ ($y > 2$) along with the sloped voltage plateau at about 1.2 V. Toward the end of the lithiation process, i.e., toward the cutoff voltage of 1.0 V (Figure 7a) and 0.8 V (Figure 7c), the heat increased slightly in the former case and more sharply in the latter case. This increase in heat is presumably related to the electrolyte decomposition in this voltage region, which is apparently more pronounced for the lower cutoff of 0.8 V. During the subsequent delithiation process (Figure 7b, d), exactly the same features were observed—just in the reversed order, i.e., peaks related to the onset of the two phase transitions and the solid-solution regime, prior to an increase toward the final cutoff of 3.0 V. Generally, the heat evolution was significantly lower, which is in good agreement with previous *operando* IMC studies on $Zn_{0.9}Fe_{0.1}O_{1-\delta}$ and $Sn_{0.9}Fe_{0.1}O_{2-\delta}$.[38,39] When lowering the lithiation cutoff to 0.01 V (Figure 7e), initially the same features were observed for the heat evolution, followed by a large heat evolution in region (C), i.e., the low-voltage region. The additional exothermic peak at about 70% state of discharge might be related to the decomposition of the electrolyte and SEI formation (just like the sharp increase toward the lower cutoff in Figure 7a,c). The very broad peak at even lower voltages (and subsequent decrease in heat evolution) might be related to the final solid-solution-type and potentially in part pseudocapacitive lithium storage, as proposed above. In fact, upon delithiation (Figure 7f), the initial very broad heat evolution feature appears to be composed of at least two features, in line with the change in slope of the corresponding voltage profile. The first one might be related to the solid-solution-type and/or pseudocapacity charge storage, while the second one has been assigned to the onset of the phase transition from $Li_yNb_2O_5$ ($y > 2$) to $Li_{1.9}Nb_2O_5$, as also observed for the other cutoff voltages. In the same line, the subsequent two peaks have been assigned to the onset of the second-phase transition from $Li_{1.9}Nb_2O_5$ to $H-Nb_2O_5$ and the solid-solution regime. Overall, the *operando* IMC results further corroborated the earlier discussed charge storage mechanism and its dependency on the degree of lithiation, and provided detailed insights into the origin of the greater heat evolution and, thus, lower EE when decreasing the cathodic cutoff voltage.

## 3. Conclusion

We successfully synthesized nanoparticulate, well-crystallized $H-Nb_2O_5$ via a hydrothermal method, followed by a calcination step at 1000 °C. Such material shows an excellent cycling stability for several hundred and even thousand cycles when setting the lower cutoff voltage to the commonly used 1.0 V. Lowering the cutoff to 0.8 V enables a slight increase in capacity, but at the expense of cycling stability. A further decrease of the lower cutoff potential yields very high capacities of, e.g., about 370 mAh $g^{-1}$ at 0.1 A $g^{-1}$, but the cycling stability decreases as well. As revealed by a comprehensive *operando* and *ex situ* investigation via a set of complementary techniques, the charge storage mechanism is basically independent from the degree of lithiation, but the continuous cycling with cutoff potentials (well) below 1.0 V

leads to an increasing disorder of the crystal structure, which eventually results in the observed fading. While lowering the cutoff is also detrimental for the overall EE and heat evolution during dis-/charge, the gain in specific energy at the full-cell level renders the application of "pulse-like" lower cutoffs potentially advantageous for its application in high-power lithium-ion batteries.

## 4. Experimental Section

*Material Synthesis and Physicochemical Characterization*: $H-Nb_2O_5$ was synthesized by a hydrothermal method, followed by calcination at 1000 °C. In more detail, 0.008 mol ammonium niobate oxalate hydrate (99.99%, Sigma–Aldrich) were dissolved in 80 mL deionized water by magnetic stirring for 1 h. Subsequently, 1.33 mL of an aqueous 2 M solution of HCl (VWR) was added dropwise into the solution. After stirring for another 1 h and 40 min in an ultrasonic bath, the solution was transferred into a Teflon-lined autoclave (Berghof BR-100). After heating at 180 °C under continuous stirring at 1000 rpm for 21 h, the resulting precipitate was washed with 250 mL deionized water and eventually dried at 80 °C overnight. The white solid was ground in an agate mortar and subsequently calcined at 1000 °C under air for 3 h with a heating ramp of 3 °C min$^{-1}$.

The as-synthesized sample was characterized by XRD in Bragg–Brentano geometry using a Bruker D8 Advance diffractometer (Cu Kα radiation, $\lambda = 0.15406$ nm). The 2θ range was from 10° to 90° with a step size of 0.04° and an acquisition time of 12.5 s per step. HRTEM was carried out using an image-side aberration-corrected FEI Titan 80–300 TEM operated at 300 kV. For these measurements, the samples were deposited on holey carbon films on Cu grids (Plano). TEM images were acquired at exposure times of about 0.5–1.0 s using a Gatan Ultrascan 1000 camera. The software Gatan Microscopy Suite was used for additional image analysis, including the Fourier transform of the HRTEM images.

*Electrode Preparation and Electrochemical Characterization*: Electrodes comprising 75 wt% of the active material, 20 wt% Super C65 carbon black (Imerys), and 5 wt% sodium carboxymethyl cellulose (CMC; Dow-Wolff Cellulosics) were prepared by dissolving the CMC in deionized water and subsequently adding the manually ground mixture of the active material and the conductive carbon. The resulting dispersion was homogenized in a planetary ball mill (Pulverisette 4, FRITSCH) for 2 h, and the thus obtained electrode slurry was cast on dendritic copper foil (99.9%, Schlenk) with a wet film thickness of 120 μm. The wet electrode sheets were dried at 80 °C for 4 h, and subsequently at ambient temperature in the dry room overnight. Circular electrodes with a diameter of 12 mm were punched and dried once more for 24 h under vacuum at 120 °C. The active material mass loading was in the range from 1.7 to 2.0 mg cm$^{-2}$.

The cell assembly was conducted in an argon-filled glove box with a water and oxygen content of less than 0.1 ppm. Three-electrode Swagelok-type cells with lithium-metal counter and reference electrodes were used for the general electrochemical characterization. Whatman GF/D glass fiber sheets served as the separator and were drenched with 120 μL of a 1 M solution of $LiPF_6$ in a 1:1 by weight mixture of ethylene carbonate and dimethyl carbonate (DMC). CR2032-type coin cells from Hohsen were assembled for the *operando* IMC experiments. Galvanostatic cycling was conducted on a Maccor battery cycler and cyclic voltammetry was performed on a Biologic VMP III. Prior to the all electrochemical tests, the cells were allowed to rest for 12 h. All electrochemical experiments were conducted at 20 °C if not specified differently.

*Operando XRD*: Operando XRD upon de-/lithiation was investigated in a 2θ range from 15° to 60° with a step size of 0.03° and an overall time of about 35 min per scan, using a self-designed two-electrode *operando* cell.[40] The electrode slurry with the same composition as the other electrodes used for the electrochemical characterization was cast directly on a beryllium window (250 μm, Materion Brush). The coated beryllium disc was dried for 2 h at room temperature and at 60 °C under vacuum

**ADVANCED
SCIENCE NEWS**

www.advancedsciencenews.com

**small
structures**

www.small-structures.com

overnight. The *operando* XRD cell was cycled using a single-channel potentiostat/galvanostat (SP-200, BioLogic).

*Operando XAS*: *Operando* XAS was conducted using pouch cells comprising either pristine electrodes or cycled electrodes and lithium-metal counter electrodes. Polyethylene fleeces (Freudenberg) were used as the separator. The *operando* XAS cell was cycled using a portable single-channel potentiostat (SP-150, BioLogic). Further experimental details are provided in the subsequent section.

*Ex Situ Characterization*: For the *ex situ* characterization via XRD, XAS, and HRTEM, the cells were stopped at specific potentials and disassembled in an argon-filled glove box. The cycled H-Nb$_2$O$_5$ electrodes were rinsed with DMC to remove the electrolyte residues and subsequently dried under vacuum and ambient temperature in the antechamber of the glove box. *Ex situ* XRD was carried on electrodes subjected to 50, 200, and 500 cycles in the fully delithiated state at 3.0 V. The electrodes were transferred to the XRD instrument in an air-tight sample holder. The measurements were conducted in the $2\theta$ range from 10° to 40°, with a step size of 0.04°.

For the *ex situ* XAS experiments, carried out in transmission mode at BM08 "LISA" at the ESRF,[41] the copper current collector was replaced by carbon paper (QuinTech) and the mass loading of the electrodes was about 7–10 mg cm$^{-2}$ to ensure a sufficient absorption. The storage ring was operated at 6.0 GeV in top-up mode with a current of 200 mA. The energy of the X-ray beam was selected using a fixed exit monochromator equipped with a pair of Si (311) crystals. Platinum-coated mirrors were used for harmonic rejection ($E_{cutoff} = 40$ keV). For all experiments, an internal niobium reference was used to correct the energy scale in the case of monochromator instabilities. The energy was calibrated based on the first inflection point of the Nb K-edge of the niobium metal reference at 18 986 eV. Standard procedures were used for pre-edge background removal and edge-step normalization using the Athena software.[42,43] *Ab initio* XANES simulation was conducted using the FDMNES code. The Nb K-edge was calculated in the photoelectron energy range of $-10 < E < 200$ eV regarding the Fermi energy level. The Hedin–Lundqvist complex potential was employed for calculating the excited states. The absorption cross section was calculated within the dipolar approximation. Note that clusters of 5 Å surrounding each nonequivalent absorbing atom were considered. The space group symmetry and constant convolution parameters were taken into account for all spectra.

*Operando IMC*: *Operando* IMC was carried out using a TAM IV microcalorimeter (TA Instruments, accuracy: ±300 nW) at a constant temperature of 25 °C. The coin cells were fixed on a custom-made rigid sample holder with a Cu-P-bronze wire (36AWG, Lakeshore) and then inserted into the calorimeter. An internal calibration of 1 h was followed, including 15 min for holding the ampoule at an equilibrium position and 45 min for the system-required signal stabilization at the measuring position. The baseline drift over the course of the measurements was lower than 5 µW. Electrochemical dis-/charge cycling tests were performed in the voltage range from 3.0 to 1.0, 0.8, and 0.01 V at a constant specific current of 0.05 A g$^{-1}$ using a BioLogic VSP multichannel potentiostat. The cells were initially allowed to rest at open-circuit voltage (OCV) conditions for 12 h for thermal equilibration. For all cutoff voltages, one complete lithiation and delithiation cycle was followed by an OCV step. The exact rest times are summarized in Table S1, Supporting Information. The variation of the active material mass loading was less than 5% to ensure comparability.

## Supporting Information

Supporting Information is available from the Wiley Online Library or from the author.

## Acknowledgements

## Conflict of Interest

The authors declare no conflict of interest.

## Data Availability Statement

The data that support the findings of this study are available from the corresponding author upon reasonable request.

## Keywords

[1] S. Fankhauser, S. M. Smith, M. Allen, K. Axelsson, T. Hale, C. Hepburn, J. M. Kendall, R. Khosla, J. Lezaun, E. Mitchell-Larson, M. Obersteiner, L. Rajamani, R. Rickaby, N. Seddon, T. Wetzer, *Nat. Clim. Change* **2022**, *12*, 15.

[2] J. Rogelj, O. Geden, A. Cowie, A. Reisinger, *Nature* **2021**, *591*, 365.

[3] B. Dunn, H. Kamath, J. M. Tarascon, *Science* **2011**, *334*, 928.

[4] M. Armand, P. Axmann, D. Bresser, M. Copley, K. Edström, C. Ekberg, D. Guyomard, B. Lestriez, P. Novák, M. Petranikova, W. Porcher, S. Trabesinger, M. Wohlfahrt-Mehrens, H. Zhang, *J. Power Sources* **2020**, *479*, 228708.

[5] M. Marinaro, D. Bresser, E. Beyer, P. Faguy, K. Hosoi, H. Li, J. Sakovica, K. Amine, M. Wohlfahrt-Mehrens, S. Passerini, *J. Power Sources* **2020**, *459*, 228073.

[6] D. Bradley, *Nature* **2008**, *451*, 652.

[7] J. Asenbauer, T. Eisenmann, M. Kuenzel, A. Kazzazi, Z. Chen, D. Bresser, *Sustainable Energy Fuels* **2020**, *4*, 5387.

[8] M. Fleischhammer, T. Waldmann, G. Bisle, B. I. Hogg, M. Wohlfahrt-Mehrens, *J. Power Sources* **2015**, *274*, 432.

[9] Y. Liu, Y. Zhu, Y. Cui, *Nat. Energy* **2019**, *4*, 540.

[10] H. Zhang, Y. Yang, H. Xu, L. Wang, X. Lu, X. He, *InfoMat* **2022**, *4*, e12228.

[11] T. Yuan, Z. Tan, C. Ma, J. Yang, Z. F. Ma, S. Zheng, *Adv. Energy Mater.* **2017**, *7*, 1601625.

[12] D. Bresser, E. Paillard, M. Copley, P. Bishop, M. Winter, S. Passerini, *J. Power Sources* **2012**, *219*, 217.

[13] D. Li, H. Zhou, *Mater. Today* **2014**, *17*, 451.

[14] Z. Hu, Q. He, Z. Liu, X. Liu, M. Qin, B. Wen, W. Shi, Y. Zhao, Q. Li, L. Mai, *Sci. Bull.* **2020**, *65*, 1154.

[15] K. J. Griffith, A. C. Forse, J. M. Griffin, C. P. Grey, *J. Am. Chem. Soc.* **2016**, *138*, 8888.

[16] J. L. Waring, R. S. Roth, H. S. Parker, *J. Res. Natl. Bur. Stand., Sect. A* **1973**, *77A*, 705.

[17] Z. Song, H. Li, W. Liu, H. Zhang, J. Yan, Y. Tang, J. Huang, H. Zhang, X. Li, *Adv. Mater.* **2020**, *32*, 2001001.

[18] Y. Zheng, Z. Yao, Z. Shadike, M. Lei, J. Liu, C. Li, *Adv. Funct. Mater.* **2022**, *32*, 2107060.

[19] S. Zhu, P. Xu, J. Liu, J. Sun, *Electrochim. Acta* **2020**, *331*, 135268.

[20] S. Ouendi, C. Arico, F. Blanchard, J. L. Codron, X. Wallart, P. L. Taberna, P. Roussel, L. Clavier, P. Simon, C. Lethien, *Energy Storage Mater.* **2019**, *16*, 581.

[21] T. Li, G. Nam, K. Liu, J. H. Wang, B. Zhao, Y. Ding, L. Soule, M. Avdeev, Z. Luo, W. Zhang, T. Yuan, P. Jing, M. G. Kim, Y. Song, M. Liu, *Energy Environ. Sci.* **2022**, *15*, 254.

[22] J. Y. Cheong, C. Kim, J. W. Jung, K. R. Yoon, S. H. Cho, D. Y. Youn, H. Y. Jang, I. D. Kim, *Small* **2017**, *13*, 1603610.

[23] J. Meng, Q. He, L. Xu, X. Zhang, F. Liu, X. Wang, Q. Li, X. Xu, G. Zhang, C. Niu, Z. Xiao, Z. Liu, Z. Zhu, Y. Zhao, L. Mai, *Adv. Energy Mater.* **2019**, *9*, 1802695.

[24] S. Li, T. Wang, W. Zhu, J. Lian, Y. Huang, Y. Y. Yu, J. Qiu, Y. Zhao, Y. C. Yong, H. Li, *J. Mater. Chem. A* **2019**, *7*, 693.

[25] T. Li, K. Liu, G. Nam, M. G. Kim, Y. Ding, B. Zhao, Z. Luo, Z. Wang, W. Zhang, C. Zhao, J. H. Wang, Y. Song, M. Liu, *Small* **2022**, *18*, 2200972.

[26] A. A. McConnell, J. S. Aderson, C. N. R. Rao, *Spectrochim. Acta, Part A* **1976**, *32*, 1067.

[27] U. Balachandran, N. G. Eror, *J. Mater. Sci. Lett.* **1982**, *1*, 374.

[28] J. M. Jehng, I. E. Wachs, *Chem. Mater.* **1991**, *3*, 100.

[29] R. M. Pittman, A. T. Bell, *J. Phys. Chem.* **1993**, *97*, 12178.

[30] M. Yang, S. Li, J. Huang, *ACS Appl. Mater. Interfaces* **2021**, *13*, 39501.

[31] Q. Deng, F. Chen, S. Liu, A. Bayaguud, Y. Feng, Z. Zhang, Y. Fu, Y. Yu, C. Zhu, *Adv. Funct. Mater.* **2020**, *30*, 1908665.

[32] P. C. Piilonen, F. Farges, R. L. Linnen, G. E. Brown, M. Pawlak, A. Pratt, *Can. Mineral.* **2006**, *44*, 775.

[33] G. M. Pugliese, F. G. Capone, L. Tortora, F. Stramaglia, L. Simonelli, C. Marini, Y. Kondoh, T. Kajita, T. Katsufuji, T. Mizokawa, N. L. Saini, *Materials* **2022**, *15*, 4402.

[34] C. Sanloup, B. Cochain, C. De Grouchy, K. Glazyrin, Z. Konôpkova, H. P. Liermann, I. Kantor, R. Torchio, O. Mathon, T. Irifune, *J. Phys.: Condens. Matter* **2018**, *30*, 084004.

[35] F. Farges, S. Rossano, *Eur. J. Mineral.* **2000**, *12*, 1093.

[36] M. Kuenzel, G. T. Kim, M. Zarrabeitia, S. D. Lin, A. R. Schuer, D. Geiger, U. Kaiser, D. Bresser, S. Passerini, *Mater. Today* **2020**, *39*, 127.

[37] J. Asenbauer, A. Varzi, S. Passerini, D. Bresser, *J. Power Sources* **2020**, *473*, 228583.

[38] J. Asenbauer, A. Hoefling, S. Indris, J. Tübke, S. Passerini, D. Bresser, *ACS Appl. Mater. Interfaces* **2020**, *12*, 8206.

[39] J. Asenbauer, A. L. Wirsching, M. Lang, S. Indris, T. Eisenmann, A. Mullaliu, A. Birrozzi, A. Hoefling, D. Geiger, U. Kaiser, R. Schuster, D. Bresser, *Adv. Sustainable Syst.* **2022**, *6*, 2200102.

[40] D. Bresser, E. Paillard, R. Kloepsch, S. Krueger, M. Fiedler, R. Schmitz, D. Baither, M. Winter, S. Passerini, *Adv. Energy Mater.* **2013**, *3*, 513.

[41] F. D'Acapito, G. O. Lepore, A. Puri, A. Laloni, F. La Manna, E. Dettona, A. De Luisa, A. Martin, *J. Synchrotron Radiat.* **2019**, *26*, 551.

[42] P. A. Lee, P. H. Citrin, P. Eisenberger, B. M. Kincaid, *Rev. Mod. Phys.* **1981**, *53*, 769.

[43] B. Ravel, M. Newville, *J. Synchrotron Radiat.* **2005**, *12*, 537.

**2300545 (11 of 11)**